







Competition between fusion and quasifission in the angular momentum dependent dynamics of heavy element synthesis reactions

T. Tanaka ¹, D. J. Hinde¹, M. Dasgupta¹, E. Williams ¹, K. Vo-Phuoc¹, C. Simenel ^{1,2}, E. C. Simpson ¹, D. Y. Jeung ¹, I. P. Carter¹, K. J. Cook¹, N. R. Lobanov ¹, D. H. Luong¹, C. Palshetkar¹, D. C. Rafferty¹ and K. Ramachandran^{1,*}

¹*Department of Nuclear Physics and Accelerator Applications, Research School of Physics, The Australian National University, Canberra ACT 2601, Australia*

²*Department of Fundamental and Theoretical Physics, Research School of Physics, The Australian National University, Canberra ACT 2601, Australia*



(Received 26 January 2023; accepted 25 April 2023; published 4 May 2023)

Background: Mass and angle distribution measurements have illuminated many aspects of the physical variables controlling quasifission. However, mapping from detection angle to reaction time is clouded by the wide range of contributing angular momenta $L\hbar$, ranging from $0\hbar$ to the maximum of the reaction ($\gtrsim 100\hbar$), which complicates the mapping, and thus limits our understanding of the reaction dynamics.

Purpose: To investigate the angular momentum dependence of the reaction dynamics in quasifission and determine the fission fragment mass evolutions in the reaction.

Method: The mass and angular distributions of products of the reactions $^{52}\text{Cr} + ^{198}\text{Pt}$ and $^{54}\text{Cr} + ^{196}\text{Pt}$ were measured. The distributions were compared with quasifission simulation results.

Results: Mass angle distributions are reproduced by utilizing a new quasifission mass evolution model, and including a mass-symmetric component associated with low L . The latter increases in yield at higher beam energy.

Conclusions: The symmetric component represents the total of slow quasifission and fusion-fission. The increase in contribution with energy above the Coulomb barrier suggests that an extra-push energy is required to achieve fusion.

DOI: [10.1103/PhysRevC.107.054601](https://doi.org/10.1103/PhysRevC.107.054601)

I. INTRODUCTION

It is now well established that reactions with different timescales contribute in nuclear collisions used to create heavy and superheavy elements. These are quasielastic scattering (timescales of $\approx 10^{-22}$ s), deep-inelastic collisions (DIC, $\approx 10^{-21}$ s), fast quasifission ($\lesssim 10^{-20}$ s), slow quasifission ($\lesssim 5 \times 10^{-20}$ s), fusion-fission ($\gtrsim 10^{-19}$ s), and fusion-evaporation reactions ($> 10^{-18}$ s) [1]. As the timescale of the reaction increases, the associated angular momentum is thought to decrease (i.e., more central collisions) [2,3]. The association between time and angular momentum can be understood in terms of the dynamics of the two colliding nuclei during the reaction. Depending on the angular momentum of the collision, the composite system undergoes rotation before either fusing or coming apart again. For fission or fission-like two-body reaction outcomes, time can therefore be extracted from the angle of the binary reaction products as long as the rotation angle θ_{rot} is less than half a rotation, $\theta_{\text{rot}} < \pi$ (timescales of $\lesssim 10^{-20}$ s). Thus key information on the reaction dynamics has come from correlated distributions of mass and angle, called mass-angle distributions (MADs) [4,5].

MAD measurements have been utilized to understand quasifission dynamics [2,6–8]. The time scales of quasifission are equivalent to the range from less than half a rotation (*fast* quasifission [9]) to several rotations (*slow* quasifission). Quasifission results in the reseparation of the systems after a certain sticking time; during contact, mass equilibration occurs between the two colliding nuclei. In fast quasifission, sticking times are short enough that full mass equilibration has not occurred, giving access to equilibration time scales [3,4,6]. The timescales and dynamics have been studied both experimentally [3–6,8,10] and theoretically [11–14].

This information has been used to understand the reaction dynamics of heavy and superheavy element synthesis reactions. In such reactions, fusion can be suppressed by 3 orders of magnitude or more [15–17] by the fast nonequilibrium quasifission (QF) [2,4] and deep-inelastic collision processes [18]. These processes are well known to interrupt heavy and superheavy elements synthesis [16,17]. Therefore, understanding how to minimise such processes via reaction selection is likely to enhance heavy and superheavy element production.

To obtain information on the angular momentum dependence of QF dynamics, including the sticking time, subtraction of MADs of $^{52}\text{Cr} + ^{198}\text{Pt}$ and $^{54}\text{Cr} + ^{196}\text{Pt}$ reactions, both forming the compound nucleus ^{250}No , at similar excitation energies E_x , have been introduced [3]. The

*Permanent address: Nuclear Physics Division, Bhabha Atomic Research Centre, Mumbai 400085, India.

choice of reactions for which the MADs were subtracted took into account several factors.

Subtracting MADs from reactions with beams and targets of different atomic number would not be suitable, since the quasifission dynamics and reaction times are known to be sensitive to the charge product in the entrance channel [19]. If MADs from the same reaction at different beam energies were subtracted, this problem is eliminated, and the angular momentum distributions would be different, giving access to the MAD of the higher angular momenta. However, the excitation energies must differ, making it difficult to attribute deduced reaction times to the effects of angular momentum alone. In future it would be interesting to see if this approach resulted in similar conclusions to the approach presented here.

Choosing reactions of different isotopes of the same elements eliminates both the above problems, since the charge product is identical, and the same excitation energies in the dinuclear system can be populated in each reaction, but with different angular momentum distributions because of the different Q values to form the dinuclear system. The only remaining issue is the possible effect of the different initial neutron numbers in the entrance channel. The effect of neutron number on the liquid drop quasifission dynamics is expected to be small [19]. Furthermore, as the two nuclei approach, neutron transfer reactions [11,14,20] are expected to rapidly equalize this difference, before the respective capture barriers are reached.

There is a potential role of $N = 28$ magicity in ^{52}Cr . It is known that magicity in the entrance channel can have a strong influence on QF [2]. However, we expect a rapid equilibration of initial N/Z asymmetry through transfer reactions [11,14,20], and the shell effects in the collision partners usually cannot survive for QF reaction time scale [20]. Since the reaction with ^{52}Cr is more N/Z asymmetric than ^{54}Cr , its $N = 28$ shell effect is not expected to be there long enough to affect the QF reaction mechanism. Thus at the time of capture, a very small residual effect of the different neutron numbers in the two reactions would be expected.

This work [3] demonstrated novel characteristics of mass evolution in the transition from fast energy dissipative DIC to QF, and provided the first direct determination of the relationship between sticking time and angular momentum. The results demonstrated both mass equilibration and fluctuations in the angular momentum dependent dynamics. Using the different projectile and target combinations with different angular momentum distribution enabled us to study them precisely with the subtraction method in Ref. [3].

Suppression of fusion due to DIC [21] has been discussed, recently including the possible role of sequential fission [22,23]. Given the findings in Ref. [22], we eliminated the influence of sequential fission by choosing $^{196,198}\text{Pt}$ targets, which have large fission barriers (23–25 MeV [24]). The fast quasifission contribution is also candidate to affect the suppression, which should be assessed with the fast quasifission equilibration model introduced in Ref. [3].

In this paper, we expand our study to reproduce unsubtracted MADs by a macroscopic reaction model using the new mass evolution model which we introduced in Ref. [3].

TABLE I. For the pairs of reactions measured in this work the center of mass energy $E_{\text{c.m.}}$, the compound nucleus excitation energy E_x , and the mean subtracted angular momenta $\langle L \rangle$ are given.

$^{52}\text{Cr} + ^{198}\text{Pt}$ $E_{\text{c.m.}} (E_x)$ [MeV]	$^{54}\text{Cr} + ^{196}\text{Pt}$ $E_{\text{c.m.}} (E_x)$ [MeV]	Sub. $\langle L \rangle$
209.5 (42.7)	213.4 (42.3)	43
215.7 (48.9)	218.1 (47.0)	50
219.0 (52.2)	222.9 (51.8)	58
223.8 (56.9)	226.7 (55.6)	64

In contrast to our previous work in Ref. [3], focusing on fast quasifission components associated with relatively larger angular momenta $L \gtrsim 30$ (timescale of $\lesssim 15$ zs), this paper includes also the slow quasifission and fusion-fission components associated with small angular momenta $L \lesssim 30$. The sticking time for $L \lesssim 30$ is found to be longer than 20 zs in several time dependent Hartree-Fock (TDHF) calculations [25–29]. This expanded study enables us to discuss the competition between fusion and quasifission in the reaction dynamics of heavy and superheavy element synthesis reactions. In addition, this study assesses the fast quasifission contribution to the suppression in capture cross section in heavy-ion induced fusion reactions.

II. EXPERIMENTAL DETAILS

The experiments were performed at the Heavy Ion Accelerator Facility at the Australian National University using pulsed beams [30,31] of $^{52,54}\text{Cr}$ (FWHM ~ 700 ps), provided by the 14UD electrostatic accelerator [32] and superconducting booster Linac [33]. The beams irradiated isotopically enriched targets of $^{196,198}\text{Pt}$ (see Table I). The target thicknesses were 190 and 40 $\mu\text{g}/\text{cm}^2$, respectively, on 20 $\mu\text{g}/\text{cm}^2$ carbon backings.

The reaction products were detected in coincidence using the ANU CUBE detector system [34]. This consisted of two large-area, position-sensitive multi-wire proportional counters, whose normals were centered at scattering angles of 45° and 90° (see Fig. 1 of Ref. [35]). The two multi wire proportional counters (MWPCs) covered laboratory scattering angles of $5^\circ < \theta_{\text{lab}} < 81^\circ$ (front MWPC) and $50^\circ < \theta_{\text{lab}} < 125^\circ$ (back MWPC), and the closest distances between detectors and target were 180 mm. The center of mass energy $E_{\text{c.m.}}$, the compound nucleus excitation energy E_x , and mean subtracted angular momenta $\langle L \rangle$ (discussed in detail later in Sec. III F) are summarized in Table I. The mass ratio $M_R = m_1/(m_1 + m_2)$, the total kinetic energy (TKE), and the the center-of-mass scattering angle $\theta_{\text{c.m.}}$ have been obtained using the fragment velocity vectors, which were determined by the time-of-flight and position information from the detectors as described in Refs. [4,19,34].

III. EXPERIMENTAL RESULTS AND ANALYSIS

A. Mass and total kinetic energy

Reaction products from several different time scales contribute to the experimental results. In order to focus on

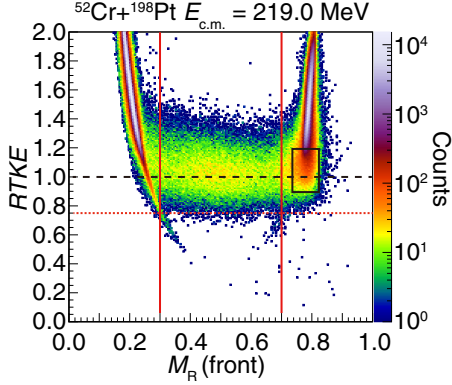


FIG. 1. RTKE vs. M_R (front) for reactions $^{52}\text{Cr} + ^{198}\text{Pt}$ $E_{c.m.} = 219.0$ MeV. M_R (front) means that the M_R for the fragments observed by the front MWPC detector which covered $5^\circ < \theta_{\text{lab}} < 81^\circ$. The red dotted lines indicate the additional gate $\text{RTKE} > 0.75$. The evidence of DIC in heavy fragments can be seen in the black box.

quasifission, the other components, such as quasielastic and DIC events, need to be removed in the analysis. Figure 1 shows fragment mass ratio M_R vs. the ratio of the measured TKE to that calculated with the M_R -dependent Viola systematics [4,36], denoted as RTKE in Ref. [37]. The data are presented for events that lie within $40^\circ < \theta_{c.m.} < 90^\circ$ in Fig. 2(c). Tails of elastic and quasielastic events displaced by experimental resolution effects are observed extending to $M_R \approx 0.35$ and $\text{RTKE} \approx 0.6$ at a level of 10^{-4} of the intensity of the elastic peak. In order to eliminate the contamination of the quasifission events, a gate $\text{RTKE} > 0.75$ is used for this analysis (horizontal red dotted line). The vertical red lines in Fig. 1 indicate values of $M_R = 0.3$ and $M_R = 0.7$, inside which the comparison was made with quasifission simulations. Based on fitting of the quasielastic scattering peak, 1σ resolutions were ≈ 0.008 for M_R and ≈ 0.19 for RTKE.

The evidence of DIC in heavy fragments can be seen at $M_R \approx 0.8$ and $\text{RTKE} \approx 1.0$ in Fig. 1 (black box). The RTKE extends down to fully damped events, (i.e., $\text{RTKE} = 1$) without significant change in the mass centroid. The mass distribution is continuous from elastic scattering to symmetric fission via quasielastic, DIC, and QF.

B. Mass and angular distributions

Because of rotation of the composite system, time translates to angle. Thus, key information on the dynamics comes from MADs. Representative MADs are shown in Fig. 2. Consistent with systematics from this entrance channel [12,19], they are dominated by fast quasifission, with no clear vertical band centered at mass symmetry from slow fission-like processes. Black and blue hatched regions correspond to lower detector efficiencies due to lower pulse height from the heavier fragment and no detector angular coverage, respectively.

A strong mass-angle correlation can be seen at $M_R \approx 0.35$ and 0.65 in the MADs of Fig. 2, meaning this is a fast process (less than a rotation) as expected, so called fast QF. M_R and RTKE (Fig. 1) show that the fast QF has evolved smoothly from DIC (which is close to the entrance-channel M_R), with

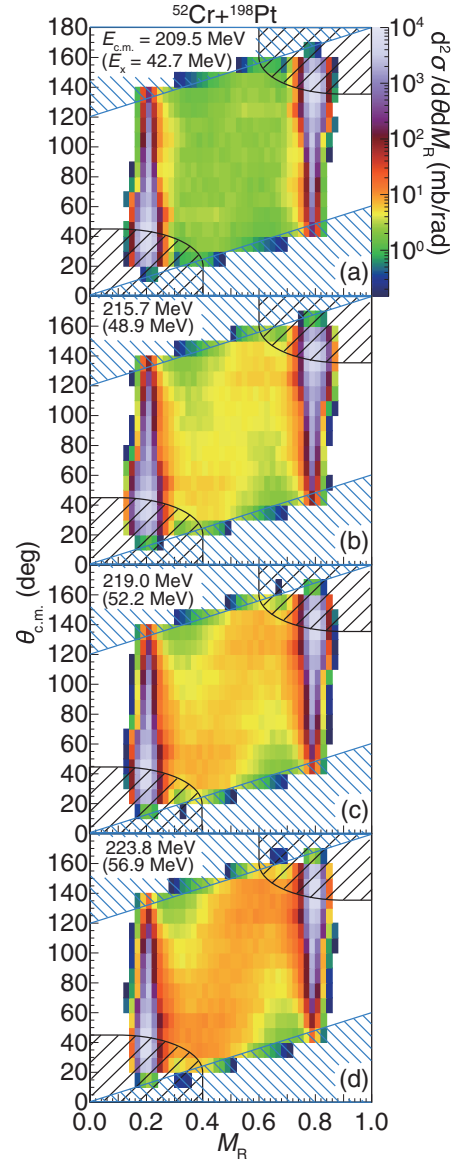


FIG. 2. Measured MADs for reactions of $^{52}\text{Cr} + ^{198}\text{Pt}$. Black hatched regions correspond to lower detector efficiencies due to lower pulse heights from the heavier fragments. The blue hatched regions correspond to no detector coverage.

no boundary seen in the MADs (Fig. 2) and $\text{RTKE}-M_R$ plot. In the mass-symmetric region ($0.4 < M_R < 0.6$), events are observed which are the sum of a fast QF and a slow QF contribution, and a component of fusion-fission which is expected to be small. The latter cannot be separated [38] as no strong vertical band centered at mass-symmetry ($M_R = 0.5$) is seen in the MADs.

C. Quasifission cross sections

Quasifission cross sections need to be extracted to determine the angular momentum L distributions (explain later in Sec. III E). The difficulty in extracting the integrated cross section originates from the shape of the angular distribution.

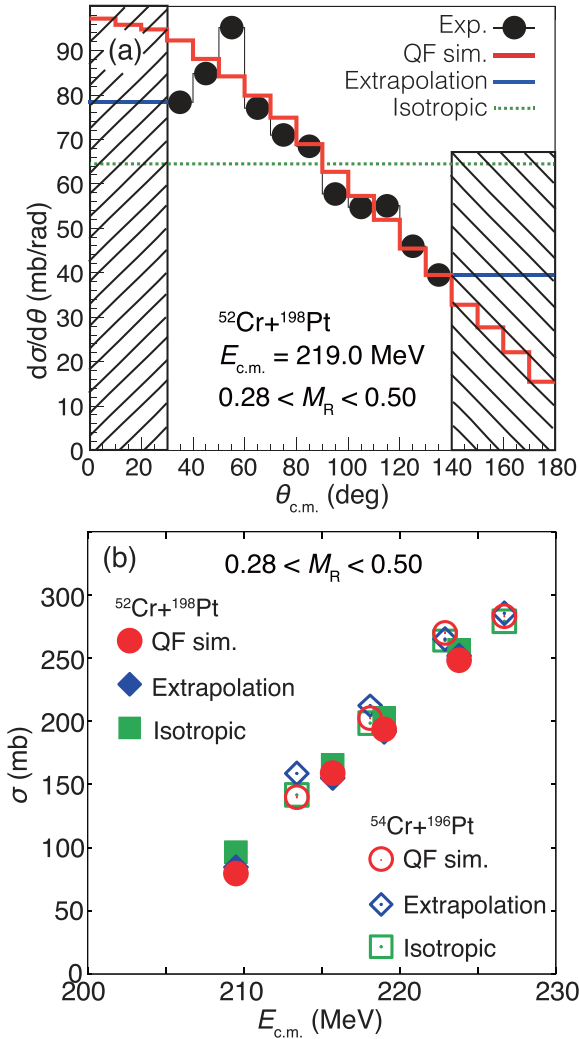


FIG. 3. (a) Angular distributions of cross sections for reaction $^{52}\text{Cr} + ^{198}\text{Pt}$ at $E_{c.m.} = 219.0$ MeV. Black hatched regions correspond to lower detector efficiencies due to lower pulse heights from the heavier fragments ($\theta_{c.m.} < 30^\circ$) and no detector coverage ($\theta_{c.m.} > 140^\circ$). (b) Total fission-like cross sections for all the measurements in this study, for the M_R range indicated.

The result indicated in Fig. 3(a) is the QF angular distribution for $^{52}\text{Cr} + ^{198}\text{Pt}$ at $E_{c.m.} = 219.0$ MeV. These are gated by $0.28 < M_R < 0.50$, complementary to the gate used in the quasifission analysis. The cross sections have been normalized by deep sub-barrier elastic scattering experimental data. The detector angular coverage ends at $\theta_{c.m.} > 140^\circ$ as indicated by the blue hatched region in Fig. 2. At forward angles $\theta_{c.m.} < 40^\circ$, yields may be reduced due to lower detector efficiencies due to lower pulse height from the heavier fragment. This corresponds to the black hatched regions in Fig. 2.

The biggest uncertainty in the quasifission cross section originates from the extrapolation to angles outside the detector coverage regions, both forward ($\theta_{c.m.} < 30^\circ$) and backward ($\theta_{c.m.} > 140^\circ$) indicated by black hatched region in Fig. 3(a). The simplest approach is to assume that the angular distributions are isotropic in $\theta_{c.m.}$. Then, we can

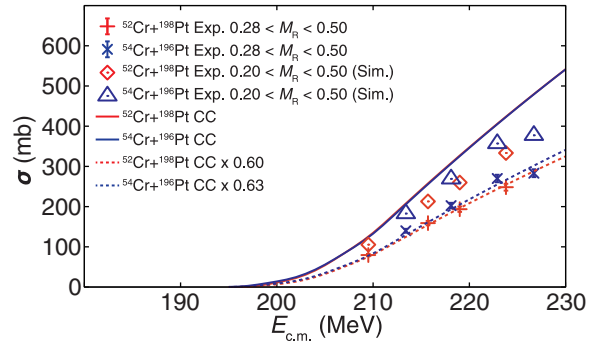


FIG. 4. Capture cross sections extracted from fission cross sections (Fission), and extrapolated with the quasifission simulation results (Sim.). The coupled-channels calculation results are indicated (solid lines), as well as the suppressed one (dotted lines). Note, majority of the red solid line ($^{52}\text{Cr} + ^{198}\text{Pt}$ CC) is overlapped by the blue solid line ($^{54}\text{Cr} + ^{196}\text{Pt}$ CC).

estimate the average of the cross section from the experimental results extracted from the detector coverage region (labelled ‘Isotropic’ in Fig. 3). Another simple method is to assume the angular distributions are constant at more forward and backward angles. Then the cross sections are estimated by utilising the cross sections of the detector edge regions (labelled ‘Extrapolation’ in Fig. 3). An empirical quasifission simulation [6,22] is also available to extrapolate the cross section to 0° and 180° . To estimate the angular distribution outside the detector coverage, we used the simulation of the fission angular distribution, without considering the fission fragment mass information. The best fit is indicated by the red line in Fig. 3, labeled ‘QF sim’. The cross sections resulting from the different extrapolations are indicated in Fig. 3(b) for both reactions. The error bar for the quasifission cross section was estimated from the distribution of the difference between the quasifission simulation and isotropic analysis and between the quasifission simulation and extrapolation analysis. The one sigma standard deviation was found to be 3.4%. This value is taken as the error bar for the cross sections in Fig. 4.

D. Comparison between the cross section and the coupled-channels calculations

To confirm the consistency of the cross sections, we compared the following cross sections: (i) Experimentally determined fission-like (fusion-fission plus quasifission) cross sections over the full angular range for $0.28 < M_R < 0.50$, (ii) Fission-like cross sections extended to the full mass and angular region ($0.20 < M_R < 0.50$ and $0^\circ < \theta_{c.m.} < 180^\circ$) making use of the new quasifission simulation (explained later in Sec. III J), (iii) Coupled-channels calculation CCFULL, (iv) CCFULL with a fitted suppression factor.

The capture barrier energies V_B were determined by fitting above barrier data with a classical barrier-passing model; $\sigma = \pi R_B^2 (1 - V_B/E_{c.m.})$, where V_B and the barrier radius R_B were free parameters. This resulted in $V_B = 203.4$ MeV for $^{52}\text{Cr} + ^{198}\text{Pt}$, and $V_B = 203.6$ MeV for $^{54}\text{Cr} + ^{196}\text{Pt}$. Coupled-channels calculations using CCFULL [39] were performed.

TABLE II. Input parameters for coupled-channel calculations based on CCFULL [39], which uses a Woods-Saxon internuclear potential, with the parameters V_0 , r_0 , and a_0 . The calculated results are shown in Fig. 4 by solid lines. For the vibrational couplings (VIB) with the ground states (g.s.), the excitation energy of a single-phonon state, E_{ph} , the deformation parameter, β_2 , and the number of phonons, N_{ph} , are shown. The values of E_{ph} and β_2 are based on Ref. [40].

$^{52}\text{Cr} + ^{198}\text{Pt}$			
$V_0 = 250.0$ MeV	$r_0 = 1.11$ fm	$a_0 = 0.65$ fm	
^{52}Cr VIB	$E_{ph} = 1.434$ MeV	$\beta_2 = 0.223$	$N_{ph} = 1$
^{198}Pt VIB	$E_{ph} = 0.407$ MeV	$\beta_2 = 0.114$	$N_{ph} = 1$
$^{54}\text{Cr} + ^{196}\text{Pt}$			
$V_0 = 250.0$ MeV	$r_0 = 1.11$ fm	$a_0 = 0.65$ fm	
^{54}Cr VIB	$E_{ph} = 0.835$ MeV	$\beta_2 = 0.250$	$N_{ph} = 1$
^{196}Pt VIB	$E_{ph} = 0.356$ MeV	$\beta_2 = 0.130$	$N_{ph} = 1$

They were constrained to reproduce the experimental capture barriers V_B by adjusting the nuclear potential radius. The couplings of ground states and first excited states of the colliding nuclei were included in the calculations. The results are indicated in Fig. 4 as coupled-channels (CC) results, and the input parameters are given in Table II.

A suppression factor S was required to reproduce the fission cross sections for $0.28 < M_R < 0.50$. $S = 0.60$ for $^{52}\text{Cr} + ^{198}\text{Pt}$ and $S = 0.63$ for $^{54}\text{Cr} + ^{196}\text{Pt}$ were used. The results reproduce the experimental fission cross sections very well. The suppression factors are in reasonable agreement with the systematics in Refs. [21,22,41].

E. Determination of the angular momentum distributions for the fast quasifission events

In order to determine the angular momenta $L\hbar$ contributing for each reaction, L distributions have been extracted from the ratio of the scattering cross section to the Rutherford cross section $d\sigma_S/d\sigma_R(\theta_{c.m.})$. This method has already been introduced in Ref. [3]. The fission-like cross section for each angular momentum $d\sigma/dL$ is defined in terms of a probability P_L . Each L value results in capture followed by fission with cross section:

$$\frac{d\sigma}{dL} = \pi\lambda^2(2L+1)P_L, \quad (1)$$

where λ is the reduced de Broglie wavelength. P_L is expected to be ≈ 1 for low L , and ≈ 0 at large L . The distribution of $d\sigma/dL$ should be roughly triangular [see Fig. 5(c)].

Scattering cross sections relative to the Rutherford cross sections $d\sigma_S/d\sigma_R(\theta_{c.m.})$ are indicated in Fig. 5(a). In the analysis, the data for $M_R < 0.28$ were used as scattering events. The ratio of scattering cross section to the Rutherford cross section $d\sigma_S/d\sigma_R(\theta_{c.m.})$ can be written $d\sigma_S/d\sigma_R(\theta_{c.m.}) = [1 - T(\theta_{c.m.})]$, where $T(\theta_{c.m.})$ is the probability for absorption at $\theta_{c.m.}$. That flux is removed from the Rutherford trajectory by complex reactions such as quasifission, so that the flux has been moved to the region $M_R > 0.28$.

The mapping was performed using the Coulomb deflection function [42,43], using $L = (D/2\lambda) \cot(\theta_{c.m.}/2)$, where

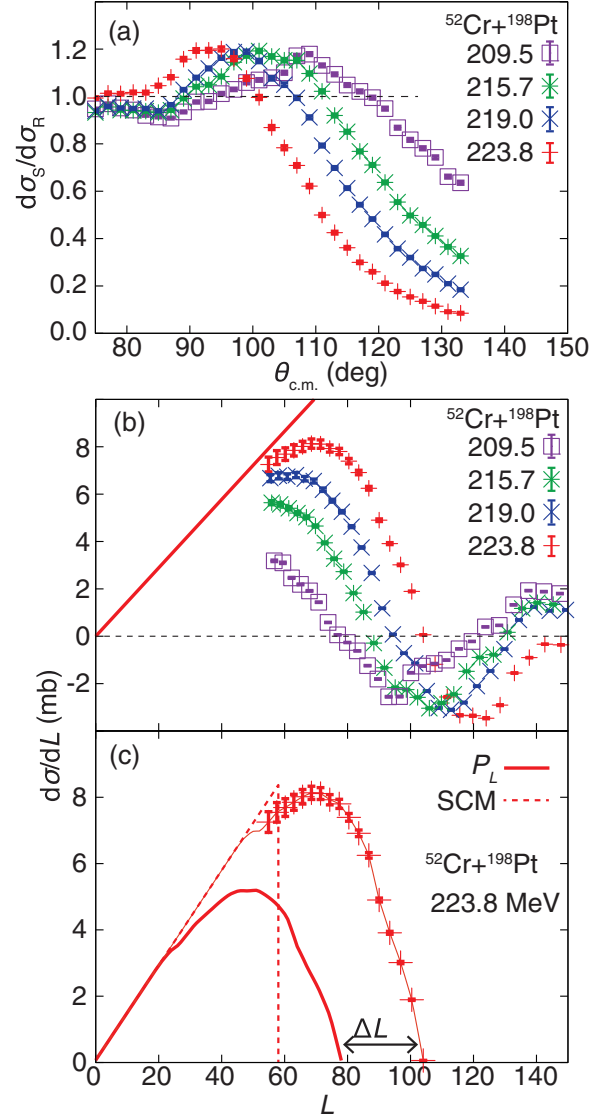


FIG. 5. (a) Scattering cross section relative to the Rutherford cross section $d\sigma_S/d\sigma_R$ with respect to $\theta_{c.m.}$. (b) Deduced cross sections $d\sigma/dL$ for each L value, from $d\sigma_S/d\sigma_R$. The red solid line indicates the $\pi\lambda^2(2L+1)$ for $^{52}\text{Cr} + ^{198}\text{Pt}$ $E_{c.m.} = 223.8$ MeV. (c) Total (symbols) and quasifission partial cross sections $d\sigma/dL$ (solid line) vs. L from P_L values shifted by ΔL (see text), and the sharp-cutoff model (SCM).

D is the distance of closest approach in a head-on collision. Figure 5(b) shows the distributions of $d\sigma/dL$. They display the expected smoothed triangular shape, but also a negative component, associated with $d\sigma_S/d\sigma_R > 1$ [Fig. 5(a)]. This feature likely results from DIC trajectories (with $M_R < 0.28$) deflected to more forward angles, resulting in higher-than-Rutherford yields. The positive values of the experimental $d\sigma/dL$ [as an example shown in Fig. 5(c)] were attributed to both DIC + QF reactions. In order to extract the $d\sigma/dL$ using Eq. (1), DIC is expected at the highest L values [43], so that we take $P_{(L-\Delta L)} = T_L$, where ΔL is a fixed L -offset chosen for each reaction to match the experimental cross section. Correspondingly the integrated cross section $\sigma =$

$\pi\lambda^2\Sigma(2L+1)P_L$. Figure 5(c) shows ΔL and $d\sigma/dL$ (solid line), adjusted to match the experimental quasifission cross section (see Sec. III C).

F. Difference of angular momentum distributions

To obtain information on the angular momentum dependence of quasifission, two MADs from the different $^{52}\text{Cr} + ^{198}\text{Pt}$ and $^{54}\text{Cr} + ^{196}\text{Pt}$ reactions with the same compound nucleus excitation energy E_x need to be subtracted. The reaction pairs are given in Table I.

In order to subtract L distributions for reactions with different λ , the cross sections need to be normalized to dimensionless reduced cross sections [16,44], that is,

$$\frac{d\tilde{\sigma}}{dL} = \frac{1}{\pi\lambda^2} \frac{d\sigma}{dL}. \quad (2)$$

Red and blue lines in Fig. 6(a) indicate $d\tilde{\sigma}/dL$ for the reactions of $^{52}\text{Cr} + ^{198}\text{Pt}$ $E_{c.m.} = 219.0$ MeV and $^{54}\text{Cr} + ^{196}\text{Pt}$ $E_{c.m.} = 222.9$ MeV, respectively. The black solid line in Fig. 6(a) is the difference between the blue and red lines, which represents the difference in angular momentum distributions between the MADs of $^{52}\text{Cr} + ^{198}\text{Pt}$ at $E_{c.m.} = 219.0$ MeV and $^{54}\text{Cr} + ^{196}\text{Pt}$ at $E_{c.m.} = 222.9$ MeV. The subtracted angular momentum distributions for all reactions are shown in Fig. 6(b).

In order to assess the robustness of the analysis, angular momentum distributions with the sharp cut off model were also calculated by adjusting the total cross section to the experimentally determined fission cross section [see Fig. 6(a) and (c)]. Arrows at the bottom in Fig. 6(b) and top in Fig. 6(c) indicate the mean values of the angular momentum distributions from the experimental scattering result [Fig. 6(b)] or with the sharp cut off model [Fig. 6(c)]. The mean values of angular momentum are similar using these two different methods. The angular momentum distributions were used as the input for quasifission simulations, and the result has been indicated in Fig. 4(d) of Ref. [3]. The trend of sticking time vs. L was consistent between the two methods, which demonstrates the robustness of this analysis method.

G. Comparison between experimental subtracted MADs and the simulation results

The subtracted MADs show us the information of angular momentum dependent reaction dynamics, such as fission fragment mass evolution with respect to the sticking time. If the subtracted MADs resulted from a single L -value, direct mapping from $\theta_{c.m.}$ to sticking time could be achieved. However, since MAD subtraction results in a range of L values (Fig. 6), quantitative analysis requires a quasifission simulation.

The details of the simulation have already been described in Ref. [3]. The $\theta_{c.m.}$ of fast quasifission events were calculated following Töke *et al.* [4,5], as implemented in Refs. [6,8,19,22]. The measured angle $\theta_{c.m.} = \pi - \theta_{in} - \theta_{rot} - \theta_{out}$ [4,19], where θ_{in} is the incoming Coulomb deflection angle up to contact, θ_{rot} is the rotation angle whilst in contact, and θ_{out} is the outgoing Coulomb deflection angle of

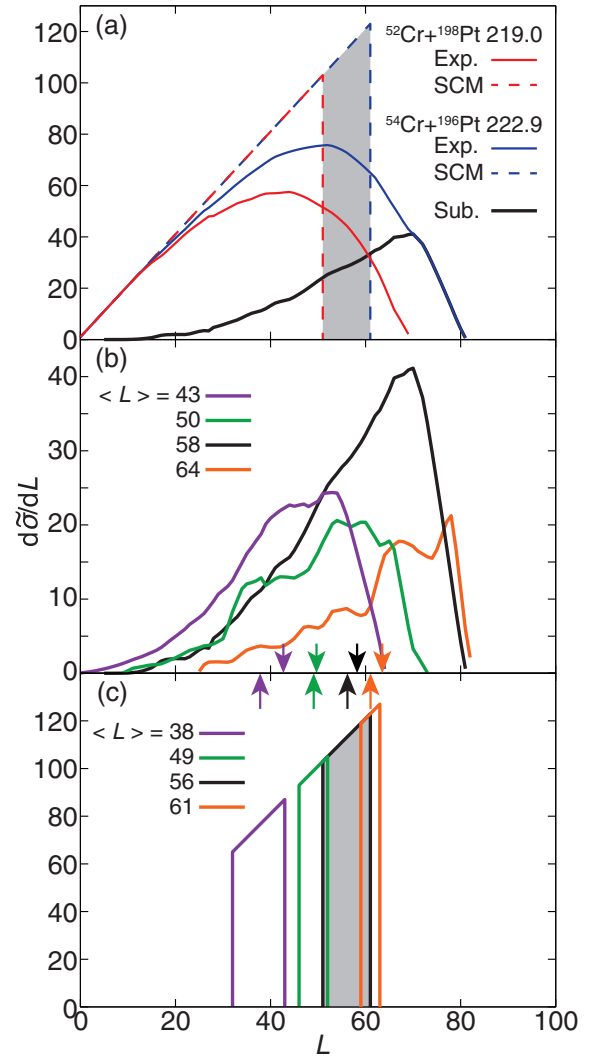


FIG. 6. (a) Experimental (solid line) and sharp-cutoff model (SCM) (dotted line) reduced cross sections $\tilde{\sigma}_L = \sigma_L/\pi\lambda^2$ vs L for the primary reactions (thin lines). The experimental difference distribution is shown by the thick black line. The SCM difference distribution is highlighted by gray color. (b) The experimental difference distributions for all reactions. The $\langle L \rangle$ are indicated by the arrows. (c) The SCM difference distributions for all reactions. The $\langle L \rangle$ indicated by the arrows are close to the $\langle L \rangle$ from experiment.

the quasifission fragments [19]. $\theta_{rot}(t_s)$ can be expressed as

$$\theta_{rot}(t_s) = \frac{L\hbar \cdot t_s}{\mathcal{I}}, \quad (3)$$

where $L\hbar$ is the angular momentum, \mathcal{I} is the mean moment of inertia and t_s is sticking time. The average moment of inertia \mathcal{I} during quasifission is then required. Time dependent Hartree-Fock (TDHF) calculations [13,45] for Cr + Pt estimated $\mathcal{I} = 2.02 \times 10^{-53}$ kg m². This is 2.04 times the spherical value [8].

The second variable in the MAD is the fragment mass ratio M_R at scission. In the previous study in Ref. [3], two mass evolution models, Töke *et al.* [4,5] and a new fast quasifission mass evolution model [3], were compared. The results

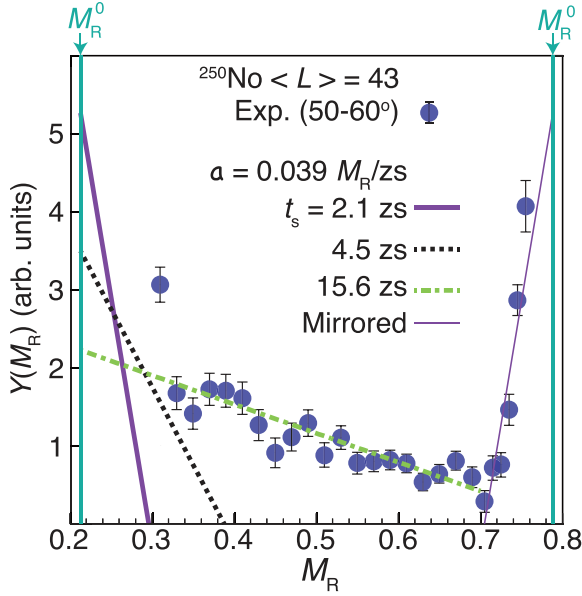


FIG. 7. Experimental yields distribution as a function of M_R (blue circles) for $50^\circ < \theta_{c.m.} < 60^\circ$ showing projectile-like (green dash-dotted line) and target-like (purple thin line) components. The lines representing the new description of time-dependent M_R distributions for three values of t_s , “Mirrored” means mirrored M_R distribution for $t_s = 2.1$ zs.

suggested that the new mass equilibration model showed better agreement with experimental results.

Experimentally, a monotonic fall in yield from the projectile and target masses towards mass-symmetry was observed in Ref. [3]. An experimental M_R distribution showing projectile-like (green dash-dotted line) and target-like (purple thin line) components is shown in Fig. 7. The lines represent the time-dependent M_R distributions for three values of t_s as detailed below. The experimental results and lines are in a good agreement, which supported a new trial function describing mass evolution in *fast* quasifission. A rapid linear fall in yield $Y(M_R)$ from M_R^0 is assumed for small t_s , with slope decreasing as t_s increases. This “fast quasifission equilibration model” is described by

$$Y(M_R) = A \left[1 - \frac{M_R - M_R^0}{at_s} \right]. \quad (4)$$

The corresponding distributions are plotted for these 3 values of t_s in Fig. 7. Here, a is the slope parameter and A provides normalization.

Subtraction of MADs has been performed after they were normalized by $\pi\lambda^2$ to cancel the difference resulting from the different de Broglie wave lengths. The sample two-dimensional results are indicated in Fig. 8(a), 8(b), and one-dimensional (1D) results for every 10 degrees are indicated in Fig. 8(e)–8(l).

The simulated MADs [Fig. 8(c) and 8(d)] were produced with the fast quasifission equilibration model described above. The variables adjusted in fits as free parameters were (i) the mean and (ii) standard deviation of Gaussian-shaped sticking

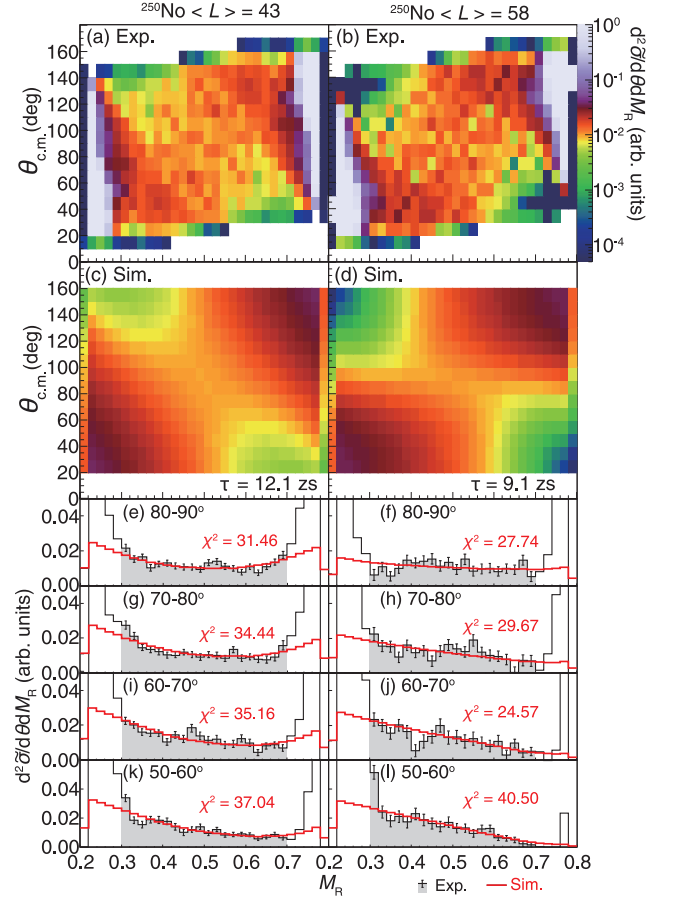


FIG. 8. Experimental subtracted MADs are shown in (a) and (b) for the indicated $\langle L \rangle$. Corresponding best-fit simulations from the fast quasifission equilibration model are shown in (c) and (d). Mean sticking times τ are given. Projected experimental (black) and simulated M_R spectra (thick red histograms) for the indicated c.m. angle ranges are given in (e)–(l), with the total χ^2 values indicated.

time t_s distributions and (iii) the slope parameter a in Eq. (4). It is important to note that only parameters (i) and (ii) affect the fragment angles. Thus, the overall angular distributions constrain these parameters. The mass distribution is determined by both the distribution of t_s and the mass evolution slope parameter a . The subtracted MADs are sensitive to the correlated angular momentum and mass evolution. A chi-squared grid search was used to find the best fit to the experimental subtracted MADs within the range $0.30 < M_R < 0.70$ and $50^\circ < \theta_{c.m.} < 90^\circ$, indicated by the grey filled region of the 1D M_R spectra shown in Fig. 8(e) to 8(l). These show that the simulation results are typically consistent within the experimental statistical error bars. The average χ^2 for each spectrum is 33, and average χ^2 per ν (degrees of freedom) is 1.9.

H. Reproducing full MADs including sticking time dependence with fast quasifission simulation

The sticking time dependence on angular momentum was discussed in Ref. [3]. We extracted the relation between mean angular momentum $L\hbar$ and mean sticking time τ from the experimental result by fitting a linear function as indicated by

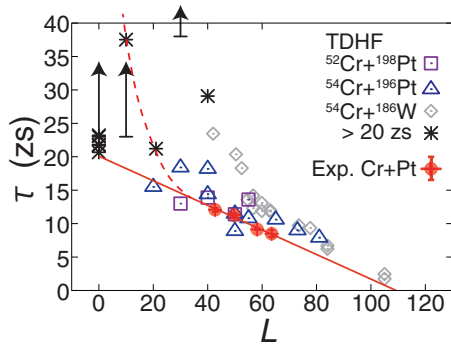


FIG. 9. Mean sticking time τ vs mean angular momentum from the experimental results published in Ref. [3] (red points). The red line indicates the best fit regarding the relation between them using the experimental points [see Eq. (5)]. Results of TDHF calculations at single L values are shown for the reactions $^{52}\text{Cr} + ^{198}\text{Pt}$, $^{54}\text{Cr} + ^{196}\text{Pt}$, and $^{54}\text{Cr} + ^{186}\text{W}$ [12,14,45]. TDHF calculation results with sticking times longer than 20 zs in the reactions of $^{40}\text{Ca} + ^{238}\text{U}$ [25–27], $^{50}\text{Ti} + ^{249}\text{Bk}$ [28], and $^{48}\text{Ca} + ^{249}\text{Bk}$ [28,29] are indicated as “ $\tau > 20$ zs”, including results giving only lower limits due to the limited time range of the calculations.

the red line in Fig. 9:

$$\tau = 20.1 - 0.184L \text{ (zs)}. \quad (5)$$

The trends of extracted values of the relations between mean angular momentum $L\hbar$ and mean sticking time τ coincide reasonably with the TDHF calculation for $^{52}\text{Cr} + ^{198}\text{Pt}$, $^{54}\text{Cr} + ^{196}\text{Pt}$, and $^{54}\text{Cr} + ^{186}\text{W}$ [12,14,45].

Based on the formula in Eq. (5), the sticking time for each simulated event was determined with the unsubtracted angular momentum distribution, examples being indicated in Fig. 6(a). The sticking time has then been used to determine the angle and mass from Eqs. (3) and (4).

The experimental full MADs are given in the top panels in Fig. 10 and the best fit simulation results are shown in the second row in Fig. 10 as Sim. (only fast QF) and by blue lines in the one-dimensional comparison figures in the bottom panels in Fig. 10. For the lowest energy $E_{c.m.} = 209.5$ MeV, the simulation reproduces the experimental result reasonably. However, for the higher energy reactions such as $E_{c.m.} = 219.0$ MeV and 223.8 MeV, the simulation was not able to reproduce the region close to mass symmetry ($M_R \sim 0.5$). It is clear that a fission contribution peaked near symmetry needs to be included from the difference between simulations (blue lines) and experiment for $E_{c.m.} = 219.0$ MeV and 223.8 MeV.

I. Near-symmetric fission contribution

Fission after forming a compound nucleus (fusion-fission) may be responsible. This component is expected to show symmetric fission without an angle correlation. In addition, a *slow* quasifission component with similar characteristics may also be present. This was not included in the *fast* quasifission mass evolution model shown in Fig. 7 and Eq. (4).

Which angular momenta might result in long sticking times? Several TDHF calculations obtained sticking times τ

longer than 20 zs for the other reactions $^{40}\text{Ca} + ^{238}\text{U}$ [25–27], $^{50}\text{Ti} + ^{249}\text{Bk}$ [28], and $^{48}\text{Ca} + ^{249}\text{Bk}$ [28,29], indicated by $\tau > 20$ zs in Fig. 9. (Note, there are no available published TDHF results for $L < 20$ for $^{52}\text{Cr} + ^{198}\text{Pt}$, $^{54}\text{Cr} + ^{196}\text{Pt}$, and $^{54}\text{Cr} + ^{186}\text{W}$ reactions.) These support the idea that the flux from $L \lesssim 30$ can result in mean sticking times $\tau > 20$ zs. Comparing the angular momentum distributions between subtracted and unsubtracted data (see Fig. 6), there is only a small contribution with $L \lesssim 30$ for the subtracted distributions and relatively significant contributions for unsubtracted distributions. Therefore, it is reasonable to attribute the symmetric fission contribution in the unsubtracted (full) MADs to the low L values. We assume these mass distributions have a Gaussian distribution, as indicated by purple thin lines in Fig. 10. The ratios of symmetric components with respect to the total events and the widths of the Gaussian distributions σ_{MR} are indicated by purple text in Fig. 10. The widths σ_{MR} are consistent with the previous expectation of the width of the fusion-fission $\sigma_{MR} \approx 0.07$ [6].

The full MADs should be better-reproduced by the simulation with the fast quasifission and the symmetric fission contribution. Four parameters were treated as free parameters: (i) Gaussian shape time distribution width of the fast quasifission equilibration model, (ii) the slope parameter a in Eq. (4), (iii) Gaussian mass width, and (iv) fraction of the Gaussian symmetric fission mode. Sticking times were calculated using the angular momentum distributions shown in Fig. 6 and Eq. (5). The χ^2 analysis provides the best fit to the experimental data. The best fits are indicated in the third row in Fig. 10 as Sim. (with Sym.) and by red lines in the one-dimensional figures in the bottom panels in Fig. 10. The contribution from the fast quasifission and symmetric fission components are indicated by green and purple thin lines, respectively. This symmetric fission component yield provides the upper limit for fusion-fission.

The fraction of slow quasifission (symmetric Gaussian component) increases with beam energy (see Figs. 10 and 11). These results suggest that although “capture” happens at the lowest beam energy we have data for (therefore, we obtained fast quasifission fragments), an “*extra-push*” energy is required to give longer sticking time components such as slow quasifission and fusion-fission. Figure 11 indicates the ratio of the longer sticking time component to the capture cross sections. Based on Bass’s interpretation [43], assuming a sharp cut-off, the slow component should be associated with the lower angular momenta. Figure 12 shows the corresponding sharp-cutoff L values for each reaction. Angular momenta with $L < 20$ are the main contributor to reactions having long sticking times (greater than one composite system rotation). In existing TDHF calculations [25–28,28,29], longer sticking times arise for smaller angular momenta ($L \lesssim 30$, see Fig. 9). The fast QF model proposed in Ref. [3] is applicable for $40 < L < 70$ since these the mean angular momenta $\langle L \rangle$ have been studied experimentally. For $L > 70$, the experimentally extracted linear function described in Eq. (5) (red solid line in Fig. 9) is in good agreement with the trend of the TDHF calculations. However, for smaller L , such as $L < 30$, another functional form is required because the reaction may not be fast quasifission anymore.

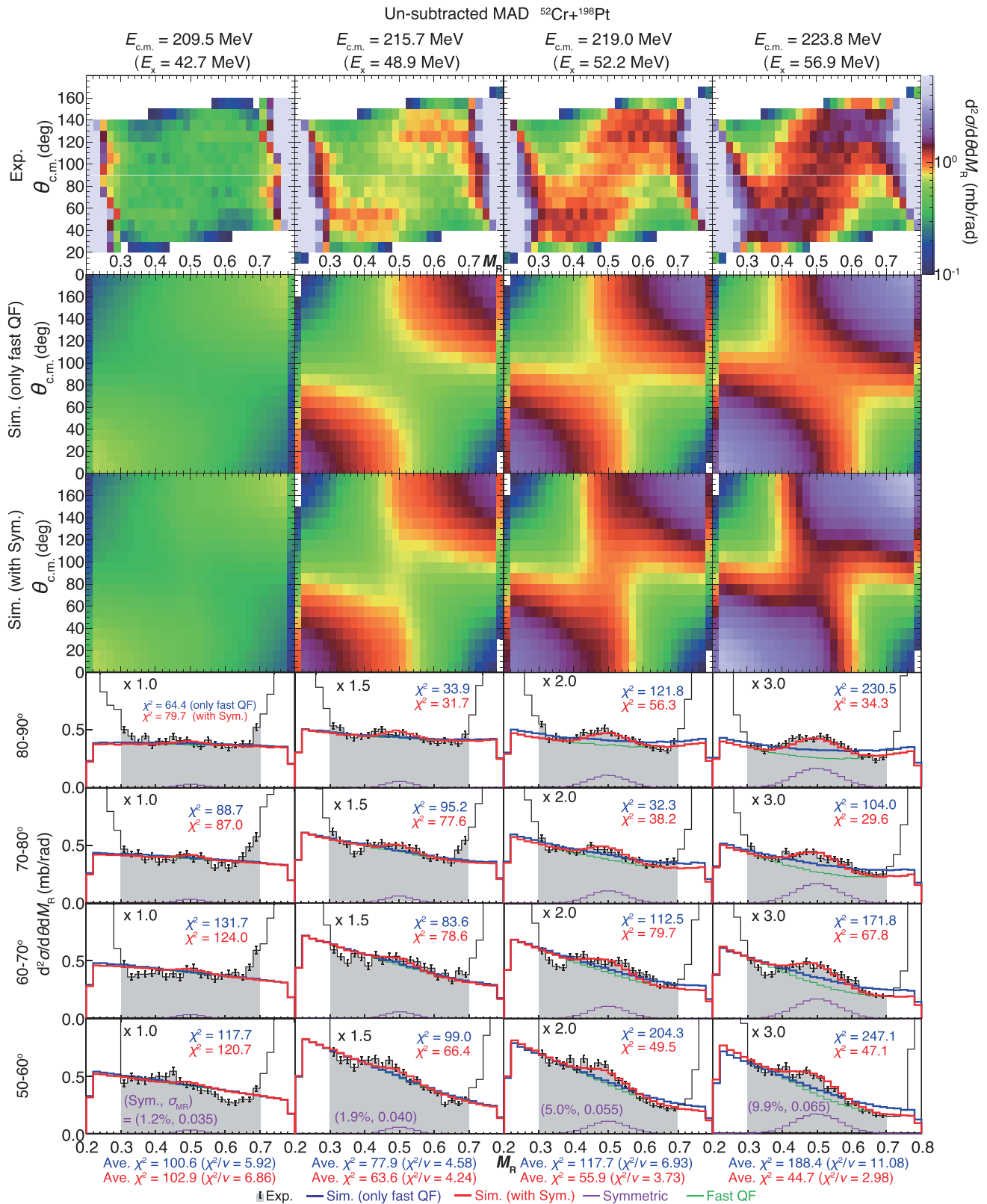


FIG. 10. Comparison between experimental results and simulation results. Experimental MADs (top panels), simulation result using only fast QF mass equilibration model (second row panels), simulation result with symmetric component (third row panels, sum of fast QF and symmetric component), and one-dimensional comparisons (bottom panels) are indicated. Statistical errors are indicated in one-dimensional comparison figures. Simulation results with symmetric contribution (red lines) are composed of sum of the fast QF simulation result (green thin lines) and symmetric contribution (purple thin lines).

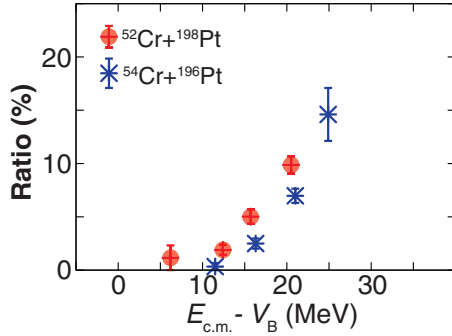


FIG. 11. Ratio of symmetric component to total fission component (quasifission and fusion-fission) (from Fig. 10) as a function of $E_{c.m.} - V_B$.

The expected function should have sticking times longer than Eq. (5) for $L \leq 30$. As an example of such a function, we indicate the red dashed line in Fig. 9. That function will be ideal for reactions well above the Coulomb barrier, such as $E_{c.m.} = 219.0$ and 223.8 MeV to reproduce the MADs including a near symmetric fission contribution. In contrast, the MAD of the lowest energy reaction $E_{c.m.} = 209.5$ MeV was well reproduced using Eq. (5) with only the fast quasifission contribution, which means Eq. (5) was still applicable for the reaction. Therefore, the slope of the red dashed line may have to transition from gentler, similar to Eq. (5), to steeper with increasing reaction energy. Further work is needed to quantify this behavior.

J. Total capture cross section utilizing quasifission simulation

One of the important observations we can make as a result of this work is that fast quasifission is present beyond the region $0.28 < M_R < 0.72$, but is generally hidden under the intense yield from quasielastic scattering events. Given the overlap between fast quasifission and quasielastic scattering

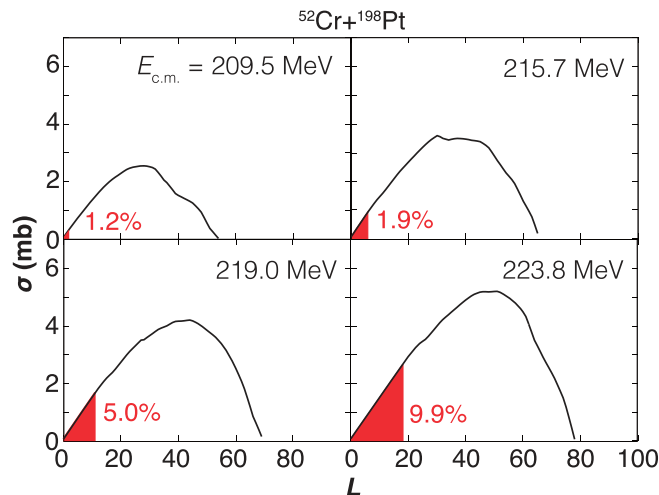


FIG. 12. Capture cross section for each angular momentum L with the equivalent cross section for the near symmetric component indicated in red.

cross sections, we were previously not able to include the fast quasifission cross-sections in our results as part of the capture cross sections. In this paper, for the first time, we can use the simulation we present here to estimate quasifission cross sections including all of the fast quasifission events. The total cross-sections for the full MAD are indicated in Fig. 4 as Exp. (Sim.). The cross sections are larger than the experimental fission cross sections extracted only in the mass region closer to symmetry. The cross sections are still smaller than coupled-channels calculations, but are significantly closer to the calculations (see Fig. 4). Combined with the proposal that sequential fission is important [22,23], this method of extrapolation using the fast quasifission model, has the potential to shed new light on the suppression of capture cross sections in heavy-ion induced fusion reactions [21,41].

IV. CONCLUSION

The mass and angular distributions (MADs) of fission fragments for the reactions $^{52}\text{Cr} + ^{198}\text{Pt}$ and $^{54}\text{Cr} + ^{196}\text{Pt}$ were measured using the CUBE fission spectrometer. These both form the compound nucleus ^{250}No . The incident energies were selected to reach the same excitation energy in the pair of reactions of different projectile and target. This enabled us to subtract the MADs from same compound nucleus and same excitation energy, but different L distributions.

The subtracted MADs reveal the L dependent sticking time, and a new mass evolution picture for fast quasifission. We extracted a linear relation between sticking time and L using the experimental results.

Using the extracted linear function and the fast quasifission mass equilibration model, we tried to reproduce the experimental unsubtracted MADs. The unsubtracted MADs show evidence for a slower more mass-symmetric component.

The unsubtracted MADs were reproduced by including a near-symmetric fission contribution in the simulation, which occurs at low L ($L \lesssim 30$) and has a longer mean sticking time τ than the linear function, i.e., $\tau \gtrsim 20$ zs. The symmetric fission contributions increased with higher beam energy. This suggests that an extra-push energy is required for fusion to occur.

The simulation results assisted in extracting the capture cross section including the fast quasifission components hidden under the elastic component, which has the potential to shed new light on the issue of suppression in capture cross section.

ACKNOWLEDGMENTS

The authors acknowledge the Australian Research Council for support through Discovery Grants No. DP200100601, No. DP190100256, No. DP190101442, No. DP170102318, and No. DE140100784. Financial support from the NCRIS HIA capability for operation of the Heavy Ion Accelerator Facility is acknowledged. The authors thank T. Kibédi for his key role in operation of the Linac.

- [1] M. Bender, R. Bernard, G. Bertsch, S. Chiba, J. Dobaczewski, N. Dubray, S. A. Giuliani, K. Hagino, D. Lacroix, Z. Li *et al.*, *J. Phys. G: Nucl. Part. Phys.* **47**, 113002 (2020).
- [2] D. J. Hinde, M. Dasgupta, and E. C. Simpson, *Prog. Part. Nucl. Phys.* **118**, 103856 (2021).
- [3] T. Tanaka, D. J. Hinde, M. Dasgupta, E. Williams, K. Vo-Phuoc, C. Simenel, E. C. Simpson, D. Y. Jeung, I. P. Carter, K. J. Cook, N. R. Lobanov, D. H. Luong, C. Palshetkar, D. C. Rafferty, and K. Ramachandran, *Phys. Rev. Lett.* **127**, 222501 (2021).
- [4] J. Töke, R. Bock, G. X. Dai, A. Gobbi, S. Gralla, K. D. Hildenbrand, J. Kuzminski, W. F. J. Muller, A. Olmi and H. Stelzer, B. B. Back, and S. Bjornholm, *Nucl. Phys. A* **440**, 327 (1985).
- [5] W. Q. Shen, J. Albinski, A. Gobbi, S. Gralla, K. D. Hildenbrand, N. Herrmann *et al.*, *Phys. Rev. C* **36**, 115 (1987).
- [6] R. du Rietz, D. J. Hinde, M. Dasgupta, R. G. Thomas, L. R. Gasques, M. Evers, N. Lobanov, and A. Wakhle, *Phys. Rev. Lett.* **106**, 052701 (2011).
- [7] D. J. Hinde, R. du Rietz, M. Dasgupta, R. G. Thomas, and L. R. Gasques, *Phys. Rev. Lett.* **101**, 092701 (2008).
- [8] E. Prasad, A. Wakhle, D. J. Hinde, E. Williams, M. Dasgupta, M. Evers, D. H. Luong, G. Mohanto, C. Simenel, and K. Vo-Phuoc, *Phys. Rev. C* **93**, 024607 (2016).
- [9] D. J. Hinde, D. Y. Jeung, E. Prasad, A. Wakhle, M. Dasgupta, M. Evers, D. H. Luong, R. du Rietz, C. Simenel, E. C. Simpson, and E. Williams, *Phys. Rev. C* **97**, 024616 (2018).
- [10] H. M. Albers, J. Khuyagbaatar, D. J. Hinde, I. P. Carter, K. J. Cook, M. Dasgupta *et al.*, *Phys. Lett. B* **808**, 135626 (2020).
- [11] K. Sekizawa and K. Yabana, *Phys. Rev. C* **88**, 014614 (2013); **93**, 029902(E) (2016).
- [12] K. Hammerton, Z. Kohley, D. J. Hinde, M. Dasgupta, A. Wakhle, E. Williams, V. E. Oberacker, A. S. Umar, I. P. Carter, K. J. Cook, J. Greene, D. Y. Jeung, D. H. Luong, S. D. McNeil, C. S. Palshetkar, D. C. Rafferty, C. Simenel, and K. Stiefel, *Phys. Rev. C* **91**, 041602(R) (2015).
- [13] C. Simenel and A. S. Umar, *Prog. Part. Nucl. Phys.* **103**, 19 (2018).
- [14] C. Simenel, K. Godbey, and A. S. Umar, *Phys. Rev. Lett.* **124**, 212504 (2020).
- [15] G. G. Adamian, N. V. Antonenko, and W. Scheid, *Nucl. Phys. A* **678**, 24 (2000).
- [16] D. J. Hinde, M. Dasgupta, and A. Mukherjee, *Phys. Rev. Lett.* **89**, 282701 (2002).
- [17] E. M. Kozulin, G. N. Knyazheva, K. V. Novikov, I. M. Itkis, M. G. Itkis, S. N. Dmitriev, Yu. Ts. Oganessian, A. A. Bogachev, N. I. Kozulina, I. Harca, W. H. Trzaska, and T. K. Ghosh, *Phys. Rev. C* **94**, 054613 (2016).
- [18] K. Banerjee, D. J. Hinde, M. Dasgupta, E. C. Simpson, D. Y. Jeung, C. Simenel, B. M. A. Swinton-Bland, E. Williams, I. P. Carter, K. J. Cook, H. M. David, Ch. E. Düllmann, J. Khuyagbaatar, B. Kindler, B. Lommel, E. Prasad, C. Sengupta, J. F. Smith, K. Vo-Phuoc, J. Walshe *et al.*, *Phys. Rev. Lett.* **122**, 232503 (2019).
- [19] R. du Rietz, E. Williams, D. J. Hinde, M. Dasgupta, M. Evers, C. J. Lin, D. H. Luong, C. Simenel, and A. Wakhle, *Phys. Rev. C* **88**, 034611 (2013).
- [20] C. Simenel, D. J. Hinde, R. du Rietz, M. Dasgupta, M. Evers, C. J. Lin, D. H. Luong, and A. Wakhle, *Phys. Lett. B* **710**, 607 (2012).
- [21] J. O. Newton, R. D. Butt, M. Dasgupta, D. J. Hinde, I. I. Gontchar, C. R. Morton, and K. Hagino, *Phys. Rev. C* **70**, 024605 (2004).
- [22] D. Y. Jeung, D. J. Hinde, E. Williams, M. Dasgupta, E. C. Simpson, R. du Rietz, D. H. Luong, R. Rafiei, M. Evers, I. P. Carter, K. Ramachandran, C. Palshetkar, D. C. Rafferty, C. Simenel, and A. Wakhle, *Phys. Rev. C* **103**, 034603 (2021).
- [23] D. Y. Jeung, D. J. Hinde, M. Dasgupta, C. Simenel, E. C. Simpson, K. J. Cook, H. M. Albers, J. Buete, I. P. Carter, Ch. E. Düllmann, J. Khuyagbaatar, B. Kindler, N. Lobanov, B. Lommel, C. Mokry, E. Prasad, J. Runke, C. Sengupta, J. F. Smith, P. Thörle-Pospiech *et al.*, *Phys. Lett. B* **837**, 137641 (2023).
- [24] P. Möller, A. J. Sierk, T. Ichikawa, A. Iwamoto, and M. Mumpower, *Phys. Rev. C* **91**, 024310 (2015).
- [25] A. Wakhle, Doctoral dissertation, The Australian National University, 2013.
- [26] A. Wakhle, C. Simenel, D. J. Hinde, M. Dasgupta, M. Evers, D. H. Luong, R. du Rietz, and E. Williams, *Phys. Rev. Lett.* **113**, 182502 (2014).
- [27] V. E. Oberacker, A. S. Umar, and C. Simenel, *Phys. Rev. C* **90**, 054605 (2014).
- [28] A. S. Umar, V. E. Oberacker, and C. Simenel, *Phys. Rev. C* **94**, 024605 (2016).
- [29] K. Godbey, A. S. Umar, and C. Simenel, *Phys. Rev. C* **100**, 024610 (2019).
- [30] N. R. Lobanov, P. Linardakis, and D. Tempra, *Nucl. Instrum. Methods Phys. Res. B* **499**, 133 (2021).
- [31] N. R. Lobanov, P. Linardakis, and D. Tempra, *Nucl. Instrum. Methods Phys. Res. B* **499**, 142 (2021).
- [32] T. R. Ophel, J. S. Harrison, J. O. Newton, R. H. Spear, E. W. Titterton, and D. C. Weisser, *Nucl. Instrum. Methods* **122**, 227 (1974).
- [33] T. Kibédi, D. C. Weisser, N. Lobanov, R. B. Turkentine, A. G. Muirhead, and D. J. Anderson, *Nucl. Instrum. Methods Phys. Res. A* **382**, 167 (1996).
- [34] D. J. Hinde, M. Dasgupta, J. R. Leigh, J. C. Mein, C. R. Morton, J. O. Newton, and H. Timmers, *Phys. Rev. C* **53**, 1290 (1996).
- [35] K. Hammerton, D. J. Morrissey, Z. Kohley, D. J. Hinde, M. Dasgupta, A. Wakhle, E. Williams, I. P. Carter, K. J. Cook, J. Greene, D. Y. Jeung, D. H. Luong, S. D. McNeil, C. Palshetkar, D. C. Rafferty, C. Simenel, and K. Stiefel, *Phys. Rev. C* **99**, 054621 (2019).
- [36] V. E. Viola, K. Kwiatkowski, and M. Walker, *Phys. Rev. C* **31**, 1550 (1985).
- [37] D. J. Hinde, D. Hilscher, H. Rossner, B. Gebauer, M. Lehmann, and M. Wilpert, *Phys. Rev. C* **45**, 1229 (1992).
- [38] D. J. Hinde, R. du Rietz, D. Y. Jeung, K. J. Cook, M. Dasgupta, E. C. Simpson, R. G. Thomas, M. Evers, C. J. Lin, D. H. Luong, L. R. Gasques, R. Rafiei, A. Wakhle, and C. Simenel, *Phys. Rev. C* **106**, 064614 (2022).
- [39] K. Hagino, N. Rowley, and A. T. Kruppa, *Comput. Phys. Commun.* **123**, 143 (1999).
- [40] S. Raman, C. W. Nestor, Jr., and P. Tikkanen, *At. Data Nucl. Data Tables* **78**, 1 (2001).

- [41] J. O. Newton, R. D. Butt, M. Dasgupta, D. J. Hinde, I. Gontchar, C. R. Morton, and K. Hagino, *Phys. Lett. B* **586**, 219 (2004).
- [42] E. Rutherford, *Philos. Mag. Ser. 6* **21**, 669 (1911).
- [43] R. Bass, *Nucl. Phys. A* **231**, 45 (1974); *Nuclear Reactions with Heavy Ions* (Springer, New York, 1980).
- [44] A. Berriman, D. J. Hinde, M. Dasgupta, C. Morton, R. Butt, and J. Newton, *Nature (London)* **413**, 144 (2001).
- [45] K. Vo-Phuoc, Doctoral dissertation, The Australian National University, 2018.